Carbon Trends 15 (2024) 100353

Contents lists available at ScienceDirect

Carbon Trends

journal homepage: www.elsevier.com/locate/cartre

Inhomogeneities across boron-doped nanocrystalline diamond films

J.J. Bennett [a,*], S. Mandal [a], D.J. Morgan [b], A. Papageorgiou [a], O.A. Williams [a], G.M. Klemencic [a,*]

[a] School of Physics and Astronomy, Cardiff University, Queen's Buildings, The Parade, Cardiff, CF24 3AA, UK
[b] Cardiff Catalysis Institute, School of Chemistry, Cardiff University, Park Place, Cardiff, CF10 3AT, UK

ARTICLE INFO

Dataset link: https://doi.org/10.17035/d.2023.0297238455

Keywords:
Boron-doped nanocrystalline diamond
Superconductivity
Inhomogeneity

ABSTRACT

For large-scale device fabrication, information about film inhomogeneities is crucial for high fabrication yield. In this work, inhomogeneities in two-inch diameter heavily boron-doped nanocrystalline diamond (BNCD) films have been studied. Two BNCD films were grown using chemical vapour deposition (CVD) with different boron-to-carbon (B/C) ratios. Their superconducting properties were measured as a function of distance from the centre of the film. The critical temperature (T_c) and critical magnetic field (H_{c2}) decreased radially outwards from the centre for both films. Raman spectroscopy, X-ray photoelectron spectroscopy (XPS), atomic force microscopy (AFM) and scanning electron microscopy (SEM) were done on the samples to pinpoint the underlying explanation for the observed behaviour. Raman spectroscopy suggested a reduction in boron concentration and diamond purity over both films while moving radially outwards from the centre. XPS data from both films, however, did not show similar behaviours to that observed from the Raman data for the B/C ratios or diamond content. The AFM scans and SEM analysis showed a decreasing grain size further away from the film centre irrespective of the B/C ratio. This is due to the film being thinner at the edges when compared with the centre of the film. Raman analysis showed that the film with the higher B/C ratio had a higher diamond purity across the film. As expected, the film with a higher B/C ratio showed a more robust superconducting behaviour. The observed reductions in boron concentration, diamond purity, film thickness and decreased grain sizes are responsible for the diminishing superconductivity at the edge of the films.

1. Introduction

Nanoelectromechanical systems (NEMS) are types of nanoscale devices that combine electrical and mechanical functions. Diamond is an advantageous material for certain NEMS because of its hardness, tensile strength and thermal conductivity [1]. With the introduction of boron dopants, diamond becomes a chemically stable electrical conductor, while heavy boron doping exceeding 10^{21} cm^{-3} induces superconductivity [2–5]. By varying other growth parameters, grain sizes in boron-doped nanocrystalline diamond (BNCD) films can also be increased or decreased. BNCD's mechanical robustness, combined with tuneable grain sizes and electrical conductivity, makes it suitable for the fabrication of complex devices. BNCD has been used to successfully fabricate devices such as coplanar microwave resonators [6], superconducting quantum interference devices (SQUIDs) [7,8], nano-mechanical resonators [9,10] and thin-film electrodes [11].

Despite the successful demonstration of BNCD for device applications, a variation in sp^2 carbon content using electrochemical techniques has been observed across BNCD films grown with different methane concentrations [12]. Therefore, the characterisation of one sample should not be used to generalise the entire film, since sp^2 carbon content will affect a boron-doped diamond electrode's performance [13,14]. Other parameters that can affect the performance of a boron-doped diamond electrode include the boron concentration [15,16] and grain size [17]. Similar to electrochemical performance, superconductivity in polycrystalline boron-doped diamond has also been shown to be affected by the doping concentration [4] and grain size [18–20]. It is therefore important to characterise inhomogeneities prior to device fabrication, particularly for large-scale applications.

In this study, inhomogeneities across two BNCD films grown with different B/C ratios have been measured and analysed. The superconducting properties and material composition of different areas from the two films are investigated. Resistance as a function of temperature, $R(T)$, and field, $R(H)$, Raman spectroscopy, X-ray photoelectron spectroscopy (XPS), atomic force microscopy (AFM) scans and scanning electron microscopy (SEM) analysis are presented as a function of radial distance from the centre of the films.

* Corresponding authors.
E-mail addresses: BennettJJ@cardiff.ac.uk (J.J. Bennett), KlemencicG@cardiff.ac.uk (G.M. Klemencic).

https://doi.org/10.1016/j.cartre.2024.100353
Received 2 January 2024; Received in revised form 9 April 2024; Accepted 9 April 2024
Available online 17 April 2024
2667-0569/© 2024 The Author(s). Published by Elsevier Ltd. This is an open access article under the CC BY license (http://creativecommons.org/licenses/by/4.0/).

2. Experimental methods

Two BNCD films were grown on commercially available silicon dioxide-buffered silicon wafers with a buffer layer thickness of 500 nm. To eliminate contaminants from the wafer surface, a 30 W oxygen plasma treatment was applied for one minute before the growth process. Oxygen plasma cleaning creates a more uniform substrate surface and optimises the surface charge which allows for high seeding densities. Silicon nitride substrates cleaned with an oxygen plasma have been shown to give the surface the most negative zeta potential compared to RCA-1 or solvent (acetone and methanol) cleaned substrates which is optimal for higher density seeding. Oxygen plasma cleaning lead to better coalescing for BNCD growth compared to the RCA-1 cleaned substrates and sharper superconducting transitions compared to both the RCA-1 and solvent cleaned substrates [21]. Given the substantial difference in surface energy between bulk silicon (2.5 J/m^2 [22]) and diamond (9.4 J/m^2 [23]), a seeding step was essential for diamond growth. Electrostatic seeding, a commonly employed method on silicon dioxide surfaces, was used for the seeding step. Detailed information on the technique and resulting seed density can be found in previously published literature [24,25]. During the seeding step, the ashed wafers were immersed in a nanodiamond solution containing positively charged nanodiamonds. Subsequently, the seeded wafers were introduced into the Seki AX6500 chemical vapour deposition (CVD) system. A gas mixture of 3% CH_4 with the rest of the gas comprising hydrogen and trimethyl boron (TMB) was used during the growth. TMB, the source of boron in BNCD, was sourced from a premixed gas cylinder containing 2000 ppm of TMB in hydrogen. Pure hydrogen from a separate bottle was added to the CVD chamber to reach the desired methane concentration. The flow of the TMB/H_2 gas mix was carefully regulated to reach the target B/C ratio. Two films were grown with a gas phase B/C ratio of 6500 ppm (henceforth referred to as 6 k) and 12800 ppm (12 k). Throughout the growth, the power and gas pressure were consistently kept at 3.5 kW and 40 torr, respectively. A dual-wavelength Williamson pyrometer was used to monitor the growth temperature, which remained at ~730 °C during the growth process.

To quantify inhomogeneities of the material properties across the BNCD films, samples were taken at regular intervals moving away from the centre of the film. Fig. 1a shows a schematic diagram of where samples A–D were taken from across a two-inch film. Centre-to-centre, each sample is spaced approximately 6–7 mm apart and the centre of sample A corresponds to the centre of the whole film. The top left corner of each sample was chipped to ensure all resistance measurements were taken in the same orientation.

Electrical transport measurements of the superconducting properties of each sample were taken using a Quantum Design Physical Property Measurement System (PPMS). The measurement leads were connected in a 4-probe Van der Pauw configuration with gold wire and silver paste bonds. All $R(T)$ data was taken by cooling the sample from 8–2 K and all $R(H)$ data was taken at 2 K by sweeping the magnetic field from 0–5 T. Raman spectroscopy of the samples was performed using a 532 nm laser in a Horiba LabRAM HR Evolution equipped with a Synapse-Plus Back-Illuminated Deep Depletion (BIDD) CCD. X-ray photoelectron spectroscopy (XPS) was performed on a Thermo Fisher Scientific K–alpha+ spectrometer. Samples were analysed using a micro-focused monochromatic Al X-ray source (72 W) using the "400–micron spot" mode, which provides an analysis defining elliptical X-ray spot of approximately 400 × 600 microns. Data was recorded at pass energies of 150 eV for survey scans and 50 eV for high-resolution scans with 1 eV and 0.1 eV step sizes respectively. Charge neutralisation of the sample was achieved using a combination of low-energy electrons and argon ions. Prior to analysis, samples were gently etched using a Thermo MAGCIS multi-mode ion source, with argon clusters with a median size of 2000 atoms per cluster. The acceleration voltage was 6 keV, yielding an energy of approximately 3 eV per nucleon. Data analysis was performed in CasaXPS v2.3.26PR1.0 [26]. Quantification was made using a Shirley-type background and Scofield cross sections, with an electron energy dependence according to the TPP-2M model. A Bruker Dimension Icon atomic force microscope was used to capture images of the sample surfaces. The microscope was operated in peak force tapping mode using a ScanAsyst tip. Scanning electron microscopy was performed on the samples using a Hitachi SU8200. The operating voltage was 20 kV and the working distance was between 10 and 11 mm.

3. Results and discussion

3.1. Superconducting properties

The superconducting properties, $R(T)$ and $R(H)$, were measured for each sample with the locations indicated in Fig. 1a. Fig. 1 shows $R(T)$ over a temperature range of 2–8 K for samples A–D from the 12 k (Fig. 1b) and 6 k (Fig. 1c) films. The insets show dR/dT for the films that show superconducting transitions within the measured temperature range. The $R(T)$ curves show an overall reduction in the superconducting transition temperature, T_c, while moving radially outwards from the film's centre. For the 12 k film, the onset of superconductivity happens in the range of 4–5 K except for sample D where the transition begins at approximately 2.5 K. On the other hand, measurements on the 6 k film only show a complete superconducting transition within the measured temperature range for sample A, which completes at slightly above 2 K. Sample B does not show a complete transition by 2 K, while sample C does not show an onset of superconductivity above 2 K. The increase in resistance with decreasing temperature seen in Fig. 1 c) for sample D is characteristic of a superconductor-insulator transition [4,27]. For all samples, the maxima in their derivatives reduce in temperature when moving radially outwards from the film centres. Overall, the 12 k film shows a higher T_c though both films follow a reduction of T_c as a function of distance from the centre of the film. Fig. 1d shows the critical temperature as a function of distance from the film centre for both films. T_c has been calculated by fitting a Gaussian curve to the dR/dT plots for samples that show a full transition in our measurement range. Samples A–C from the 12 k films show complete transitions which decrease in temperature when moving radially outward from the centre of the film. Only sample A from the 6 k film has a complete transition and this T_c is lower than any critical temperatures measured from the 12 k film.

To further characterise the superconductivity as a function of distance from the film centre, Fig. 2 shows $R(H)$ over an applied magnetic field range of 0–5 T for samples A–D from the 12 k (Fig. 2a) and 6 k (Fig. 2b) films. For each measurement, the sample temperature was maintained at 2 K. The insets show dR/dH for those samples exhibiting a magnetic field-induced transition within the measured field range at 2 K. Similar to the $R(T)$ measurements shown in Fig. 1, Fig. 2 shows a reduction in the upper critical field, H_{c2}, for samples further away from the film centre. Fig. 1a shows an incomplete superconducting transition as a function of temperature for sample D due to the 2 K base temperature of the PPMS. Consequently, a partial field-induced transition can be seen in Fig. 2a for sample D measured at 2 K. Furthermore, in Fig. 1b no superconducting transition as a function of temperature can be seen for samples C and D, which are taken furthest from the film centre. As a result, there is no field-induced transition visible in Fig. 2b. Samples measured from the 12 k film show a higher H_{c2} though both the 12 k and 6 k films show a reduction of H_{c2} further away from the film centre. In Fig. 2c the upper critical field is plotted as a function of distance from the centre of each film which has been calculated by fitting a Gaussian curve to the dR/dH plots for samples that show a full transition in our measurement range. The behaviour of H_{c2} as a function of distance from the film centre is the same as T_c for both films.

3.2. Raman spectroscopy

To investigate the potential causes for the observed variation of the superconducting properties of the films as a function of distance from

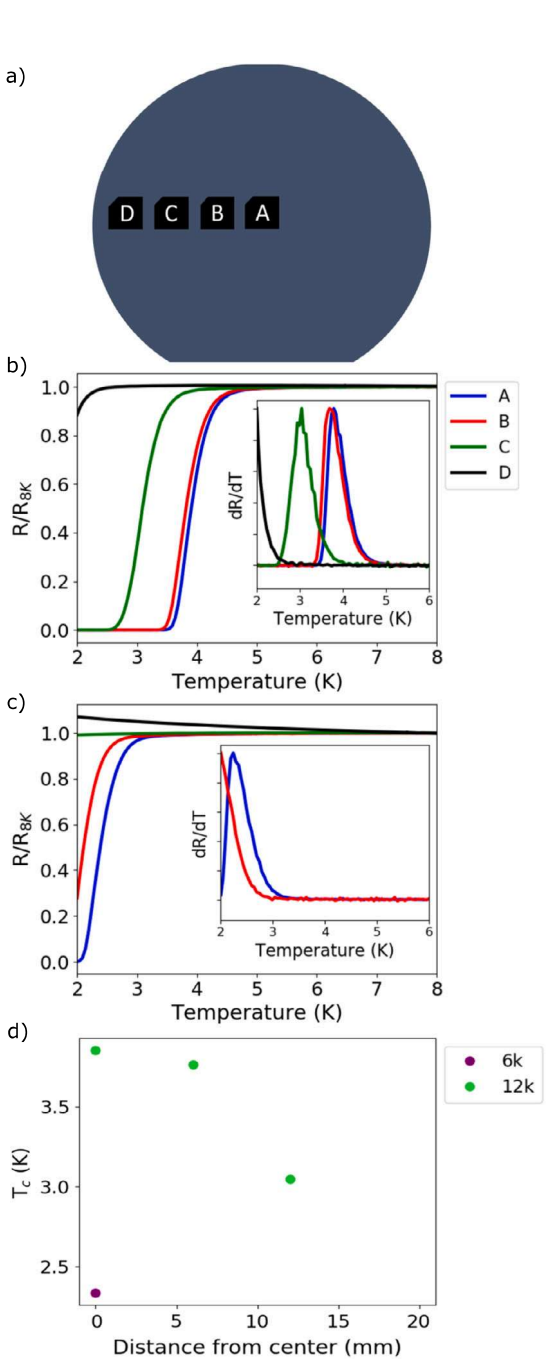

Fig. 1. A schematic diagram showing the different samples of each BNCD film under investigation, labelled A–D. Resistance as a function of temperature, $R(T)$, for samples A–D from both films and T_c as a function of distance from the centre of the film. a) The diagram shows the location of the four samples measured across each (12 k or 6 k) two-inch BNCD film. Sample A is exactly in the centre of the film, and the centres of each sample are spaced approximately 6–7 mm apart. Each sample has a notch in the top left corner to ensure that all electrical measurements were taken in the same orientation. $R(T)$ for **b)** the 12 k film and **c)** the 6 k film have been normalised to $R_{8\,\mathrm{K}}$. The insets show dR/dT normalised to $(dR/dT)_{\max}$. dR/dT for samples C and D from the 6 k film are not shown as there are no superconducting transitions within the measured temperature range. **d)** T_c as a function of distance from the centre of the film for both films where T_c has been determined by Gaussian fits to the normalised dR/dT plots. Samples that do not have a complete transition in our measurement range have not been plotted and error bars are smaller than the symbols.

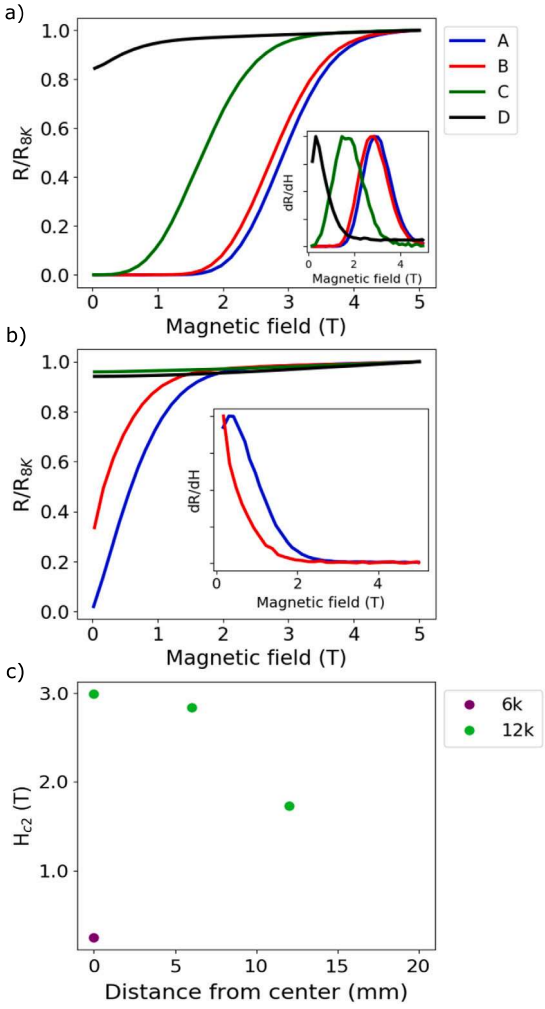

Fig. 2. Resistance as a function of magnetic field, $R(H)$, for samples A–D from both films taken at 2 K and H_{c2} as a function of distance from the centre of the film. $R(H)$ for **a)** the 12 k film and **b)** the 6 k film have been normalised to R_{5T}. Insets show dR/dH normalised to $(dR/dH)_{\max}$. dR/dH for samples C and D from the 6 k film are not plotted as there are no transitions within the measured range. **c)** H_{c2} as a function of distance from the centre of the film for both films where H_{c2} has been determined by Gaussian fits to the normalised dR/dH plots. Samples that do not have a complete transition in our measurement range have not been plotted and error bars are smaller than the symbols.

the film centre, Raman spectroscopy was used to study the material composition. Raman spectra were deconvoluted, then numerical analysis was used to calculate the boron concentration and diamond content on the spots measured in each sample. Fig. 3a shows an annotated Raman spectrum of sample A from the 12 k film. Two broad peaks are observed at roughly 450 cm^{-1} (dA), 1200 cm^{-1} (dC) and an asymmetric peak at 1290 cm^{-1} (dB), which are all commonly observed in highly boron-doped diamond [28]. The origin of the dA peak is believed to result from boron dimmers or clusters of boron [29,30], while the dC peak is thought to originate from a maximum in diamond's phonon density of states [30,31]. For undoped diamond, the zero phonon line (ZPL) occurs at roughly 1332 cm^{-1} as a sharp Lorentzian peak, though this changes with boron doping [32]. The boron atoms behave as p-type dopants and increase the conductivity, which modifies the ZPL to an asymmetric line shape (peak dB) while also reducing the wavenumber shift and peak intensity. This change to a Fano line shape is known as the Fano effect and is caused by interference between the ZPL and the continuum of electronic transitions that result from metallic doping [33]. At roughly 1400 cm^{-1} and 1600 cm^{-1} there are two broad peaks associated with non-

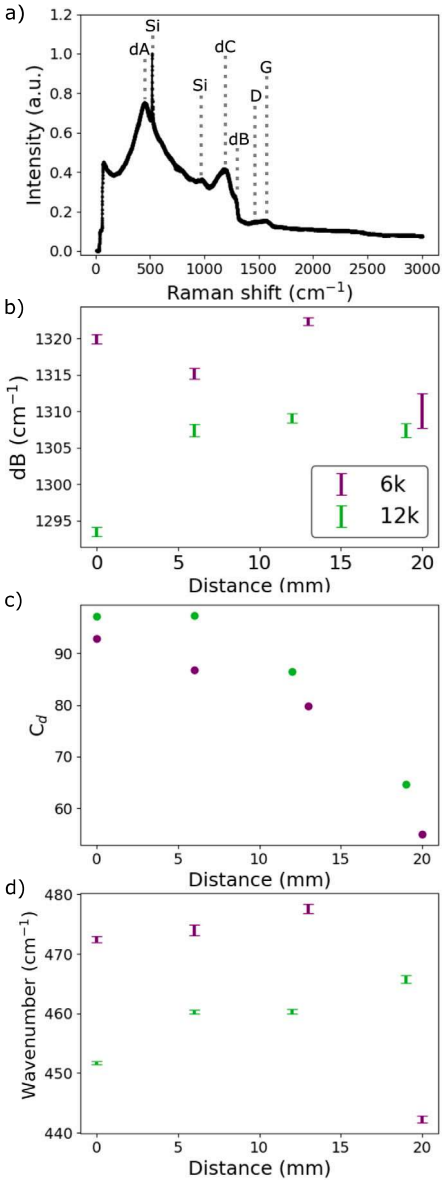

Fig. 3. An annotated Raman spectrum and Raman analysis for all samples. **a)** An annotated Raman spectrum for sample A from the 12 k film normalised to the first-order silicon peak. **b)** dB as a function of the distance from the film centre for all samples from the 12 k (green) and 6 k (purple) films. **c)** C_d as a function of distance from the film centre where the error bars are smaller than the symbols. **d)** Lorentzian wavenumber from the fitted dA peaks as a function of distance from the film centre. All Raman measurements were taken with a 532 nm laser.

diamond carbon known as the D and G-peaks respectively [34]. Finally, the peaks originating from the silicon substrate appear at approximately 520 cm^{-1} (first order) as a sharp peak and 980 cm^{-1} (second order) as a much broader peak [35]. The fitted dB peak (Fano resonance) for each spectrum is plotted in Fig. 3b as a function of distance from the film centres (see Fig. 1a for the diagram of the samples relative to the centre of the film). Heavier boron doping leads to a larger reduction of the Raman shift of the Fano resonance [36]. The Raman shift position of the dB peak is also very susceptible to stress; tensile stress reduces the Raman shift wavenumber, while compressive stress increases the Raman shift wavenumber [37–39]. The behaviour seen in Fig. 3b indicates a change in one, or both of these parameters (B/C and stress). For the 12 k film, the Fano resonance increases from A to B and then plateaus. The intensity of the Raman spectrum of sample D from the 6 k film was incredibly weak apart from the silicon peaks (Fig. S1b); this decrease in intensity will lead to a high signal-to-noise ratio, thus reducing the accuracy of the Fano fitting leading to larger error bars. The diamond content, C_d, in the samples was estimated using the method given in [38]:

$$C_d = 100A_d/(A_d + \frac{\sum A_i}{50}), \quad (1)$$

where A_d is the area of the fitted diamond peak (dB) and A_i is the sum of the areas from the fitted D and G peaks [40]. C_d is plotted as a function of distance from the film centres in Fig. 3c, which shows an overall reduction of diamond over the films as a function of distance from the film centre. To measure the variation in B/C ratio across the films, the dA peak was fitted with a Lorentzian line shape and analysed as shown by Bernard et al. [41], who concluded that a higher B/C ratio leads to a reduction in the Lorentzian wavenumber. Fig. 3d shows the calculated B/C ratio as a function of distance from the film centres for both the 12 k and 6 k films. The increasing Lorentzian wavenumber with distance from the centre indicates a reduction in boron concentration across the film. The wavenumber of the 20 mm sample from the 6 k film, however, deviates considerably from the established increase from the film centre (Fig. 3d). The intensity of this sample's Raman spectrum (Fig. S1b) was very weak compared to the samples that were taken closer to the film centre. The large decrease in signal intensity again reduces the accuracy of the data analysis. The analysis in Fig. 3b does not show the same behaviour as Fig. 3d; these differences may be due to stress in the samples. The Raman shift position of the dB peak is very susceptible to stress [37], while the peak position of dA is not. The behaviour in Fig. 3b could therefore be a result of B/C and stress variation, whereas Fig. 3d only shows a reduction in B/C. The deconvoluted dA peak was used to calculate the boron concentration, [B], in each of the spots measured on the samples. The boron concentration was estimated using the linear relationship between the dA peak wavenumber and [B] calculated by Mortet et al. [42],

$$[B] = -6.99 \times 10^{19}\omega + 3.57 \times 10^{22} \quad (2)$$

The calculated values are given in Table 1 and equation (2) predicts the magnitude of boron concentration is higher in the 12 k film compared to the 6 k film. A reduction in boron concentration when moving radially outwards from the centre of each film is calculated. Given the poor accuracy of the dA peak position for sample D from the 6 k film, it is not possible to accurately calculate the boron concentration. It is very likely to have a lower boron concentration than sample C from the same film, as is the case for samples C and D from the 12 k film. Calculating the boron concentration using the shift of the dA peak can potentially underestimate the boron concentration compared to other methods [43], since it only takes into account boron affecting the dA peak. Our dA peak positions are all within the range used by Mortet et al. to establish the relationship between [B] and the wavenumber of dA. We believe that this alignment with established literature reinforces the validity of our analysis and enhances the accuracy of our findings. The reduction of T_c and H_{c2} for samples moving radially outwards from the film centre (Fig. 1 and Fig. 2) and the Raman analysis (Fig. 3d) suggests there is a decrease in boron concentration across the film, which has been shown to strongly affect the transition temperature of superconducting boron-doped diamond [4,5,44,45]. For boron-doped diamond, a high concentration ($n_B \geq 1.3 \times 10^{21}$ cm^{-3}) of boron is required for superconductivity [3]. Given the variation in boron concentration from the Raman analysis (Fig. 3d, it is possible that the lower B/C measured at the spots on samples C and D from the 6 k film indicates that both of the whole samples have fallen below the B/C threshold required for observable superconductivity in diamond over our measurement range, as seen in Fig. 1 and Fig. 2. Additionally, the observed reduction of diamond purity further from the film centres will also contribute to the diminishing superconducting properties [46].

3.3. X-ray photoelectron spectroscopy

XPS measurements were performed on the samples to investigate if the surface properties show similar inhomogeneities across the films as revealed by the electrical and Raman measurements. The survey and C 1 s spectra were measured and analysed for all samples. An annotated survey spectrum for sample A from the 12 k film in Fig. 4a shows peaks for oxygen (O 1 s), nitrogen (N 1 s), carbon (C 1 s), boron (B 1 s) and silicon (Si 2p). The C 1 s peak from the same sample is shown deconvoluted and annotated in Fig. 4b. The largest component at ~285 eV is attributed to C-C bonds. Five other peaks were also fitted with binding energies of ~283.5, ~286, ~287, ~288 and ~290 eV. The ~283.5 eV peak is attributed to carbides [47]. Peaks with binding energies of ~286, ~287, ~288 and ~290 eV are attributed to alcohol, ether, carboxyl and carbonate groups respectively [47]. To determine the B/C ratio, the survey spectra of each sample were used to divide the percentage of the total B 1 s component by the percentage of the total C 1 s component. In Fig. 4c, the calculated B/C ratio is plotted as a function of distance from the film centre for both the 12 k and 6 k films. The boron concentration varies over the surface and is higher in magnitude on the 12 k film and, to a greater extent, decreases with distance from the film centre. Besides the large increase of the B/C ratio from samples A to B in the 12 k film, there is a reduction from samples B to D. Finally, the deconvoluted C 1 s peaks were used to determine the percentage of diamond in each sample, shown in Fig. 4d. There is a less than 5% variation in diamond percentage across all sample surfaces apart from the roughly 10% increase between samples A and B in the 12 k film. This analysis also shows a higher relative amount of diamond on the surface of the 6 k film. Similar variations in sp^3 carbon content have been seen in boron-doped carbon nanowalls studied using XPS [48], where the boron concentration was in the range of $0 < B/C < 5000$ ppm. While the analysis of the Raman spectra showed a reduction of boron concentration and diamond purity moving radially outward from the film centre, the XPS analysis does not show similar behaviour. The probable explanation for this deviation may be due to the varying depths to which XPS and Raman spectroscopy probe the sample. XPS has a surface penetration depth of ~5 nm, which is much smaller relative to the complete penetration achieved by Raman spectroscopy (microns) [49]. This means that while the Raman spectra will probe the bulk of the sample, XPS only measures the first few layers at the surface of the sample. The growth of polycrystalline diamond films follows a well-established Volmer-Weber [50,51] growth mechanism in the initial phase of growth followed by a van der Drift columnar growth mechanism [52], which gives rise to somewhat conically shaped diamond columns [53]. The growth mechanism therefore results in large grains at the surface which obscure smaller grains underneath (smaller grains lead to a lower diamond/non-diamond ratio). The shallow depth sensitivity of XPS may therefore result in the observed discrepancies in diamond properties across the films.

3.4. Atomic force microscopy

The sample surfaces were studied using AFM to establish a relationship between the surface morphology and the observed inhomogeneities in resistivity, B/C ratio, and diamond content in the films while moving radially outwards. The AFM images from each sample are shown in Fig. 5 where the scale bar to the right of each image indicates the variation in surface height. In all cases, the samples show a granular structure. For the 12 k film, the grain height is reduced with distance from the centre of the film. Under the same growth conditions, it has been shown that the grain size at the surface has a direct correlation with film thickness [54]; with this in mind, it is evident from the AFM images that there is a considerable thickness variation between the centre and the edge of both films. An increase in the number of grains at the surface can be seen in both films further away from their centres. Sample D from the 12 k film and samples C and D from the 6 k film have more grains at the surface for the same measurement area as compared to other samples of the same film. Additionally, sample D from the 6 k film has a much smoother surface and less defined grain boundaries. Fig. 1 and Fig. 2 showed no superconducting transitions for these three samples (sample D from the 12 k film and samples C and D from the 6 k film). A reduction in sample thickness has previously been shown to reduce the T_c of polycrystalline boron-doped diamond films [5,20,55]. Thinner BNCD films grown under the same conditions are comprised of smaller grain sizes [20,54], which in turn increases the volume of grain boundaries and further weakens superconductivity [19]. Since grain boundaries contain non-diamond carbon [53,56], this explains the reduced C_d seen in Fig. 3c. The observed increase in grain boundary volume combined with the reduced B/C ratio across

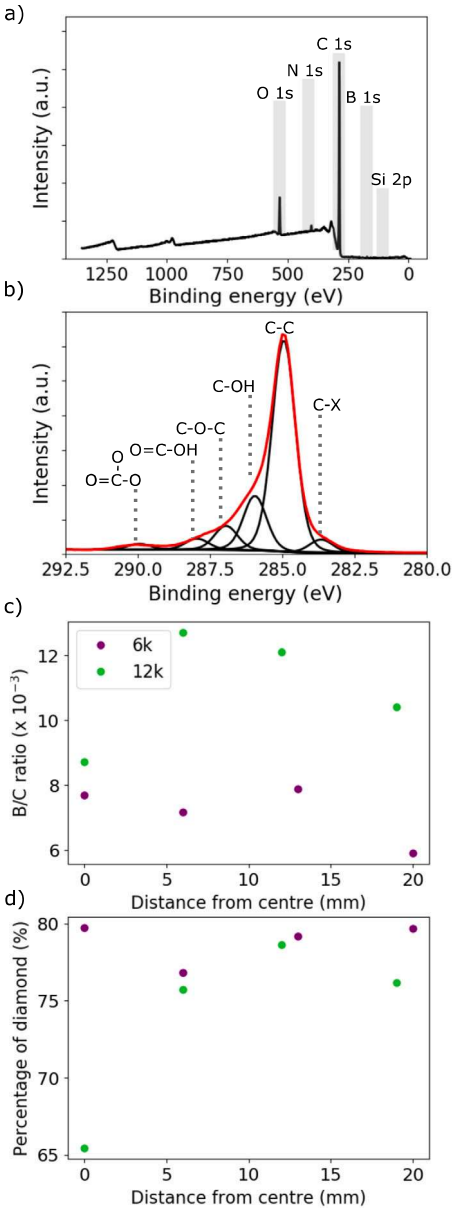

Fig. 4. An annotated X-ray photoelectron spectroscopy (XPS) survey, C 1 s spectrum, and XPS analysis for all samples. a) Annotated XPS survey spectrum for sample A from the 12 k film. **b)** Annotated C 1 s spectrum for sample A from the 12 k film indicating all bonding states of carbon present in the sample. **c)** Boron-to-carbon (B/C) ratio as a function of distance from the film centre for all samples from the 12 k (green) and 6 k (purple) films. **d)** Percentage of diamond as a function of distance from the film centre for all samples.

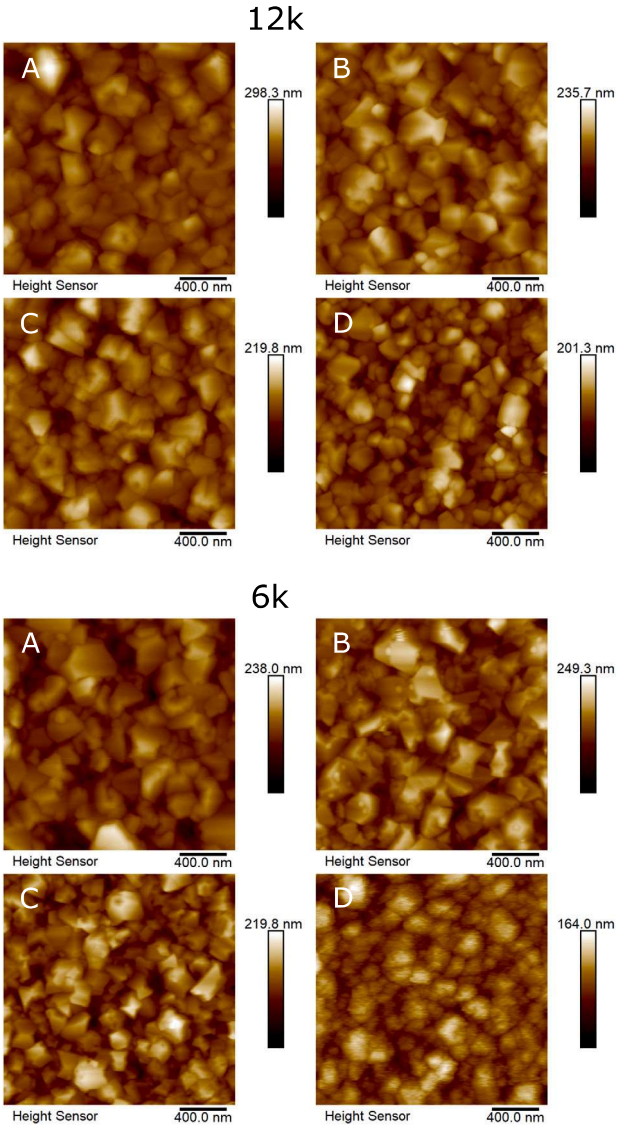

Fig. 5. Atomic force microscopy (AFM) images of samples A–D from the 12 k (top) and 6 k (bottom) films. The scale bar to the right of each image indicates the variation in surface height. Each sample shows a granular structure, with grain boundary density increasing with distance from the film centre.

the films is responsible for the reduction of T_c and H_{c2}. Inhomogeneous nanodiamond seeding density could be a contributing factor to our results; Tsigkourakos et al. [57] found a variation in the seeding density for three different spin-seeded wafers at different distances from the centre of their films. Lower seeding densities can impact the ability of the grains to coalesce and result in a poorer-quality film.

3.5. Grain analysis

Following AFM measurements the grains were analysed numerically. The grain area distributions have been determined using SEM images and are shown in Fig. 6. The grain area distributions for samples further away from the film centre do not contain the larger grain areas which are seen in samples closer to the centre. In both the 12 k film (Fig. 6a) and 6 k film (Fig. 6b), the largest grain area distributions are seen in sample A (closest to the centre) which decrease progressively to sample D (furthest away from the centre). The mean grain diameter in each sample has been calculated from these distributions and the values for each sample are given in Table 1. Despite sample B from the 6 k film having the largest mean grain diameter, the superconductivity in

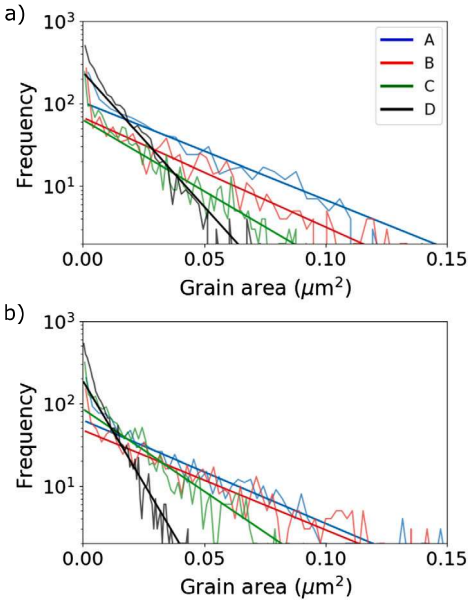

Fig. 6. Grain area distributions for samples A–D from both films determined from SEM analysis. a) The grain area distribution for samples the 12 k film. **b)** The grain area distribution for samples the 6 k film.

this sample is still limited by the low boron concentration. The reducing grain area distributions suggest the film is becoming thinner in the measured area [20,54]. Sample D from both films show much steeper gradients in the line of best fit, relative to other samples, for their distribution which is indicative of much smaller grain areas.

In Fig. 7 the dependence of the T_c, H_{c2}, C_d and [B] are plotted as a function of the mean grain diameter. Fig. 7a only shows samples that showed a complete transition in our measurement range and shows that the critical temperature is higher in samples with larger grains. Only one sample from the 6 k film showed a complete transition, with a T_c lower than all samples from the 12 k film. The same can be said for H_{c2} (Fig. 7b), which shows that samples from the 12 k film have higher upper critical fields, compared to the 6 k film, that increase as the mean grain diameter increases. More grain boundaries lead to weaker superconductivity in BNCD [19,20], so larger grains will result in fewer grain boundaries and a more robust superconducting state. Fig. 7c shows that C_d increases as the mean grain diameter increases. Larger grain sizes reduce the volume of grain boundaries and therefore reduce the quantity of non-sp^3 carbon in that area. Hence, both films show increased sp^3 content in samples with larger mean grain diameters. The calculated boron concentration increases as the mean grain diameter increases in the 12 k film (Fig. 7d). There is less variation in [B] in samples from the 6 k film and the magnitude is lower compared to the 12 k film due to a lower B/C during growth. The poor signal-to-noise ratio for the smallest mean grain diameter in the 6 k film (sample D in Fig. S1b) results in a highly inaccurate calculated [B], so it is not included in the figure. The boron concentration is higher in samples with larger mean grain diameters, which are the samples closer to the centre of the film. Higher boron concentrations coupled larger grain sizes and higher diamond purity towards the centre of the films results in a region with a more robust superconducting state, leading to higher T_c and H_{c2}.

4. Conclusion

In this work, two BNCD films (12 k and 6 k) were grown with varying B/C ratios. Electrical and structural measurements done on the samples from various points, while moving radially outwards from the centre, reveal significant inhomogeneities in the film properties. The electrical characterisation of the samples reveals a variation in superconducting transition temperature and critical field. The transition

Table 1
Superconducting and structural parameters obtained for each sample from the 6 k and 12 k films.

Sample	T_c (K)	H_{c2} (T)	C_d	[B] (cm^{-3})	Mean grain diameter (nm)
6 k A	2.33	0.25	92.77	2.68×10^{21}	153.17
6 k B	-	-	86.78	2.57×10^{21}	167.76
6 k C	-	-	79.77	2.32×10^{20}	116.69
6 k D	-	-	55.02	-	76.96
12 k A	3.86	2.99	97.15	4.13×10^{21}	158.32
12 k B	3.77	2.84	97.3	3.53×10^{21}	152.03
12 k C	3.05	1.73	86.5	3.52×10^{21}	128.21
12 k D	-	-	64.70	3.14×10^{21}	99.01

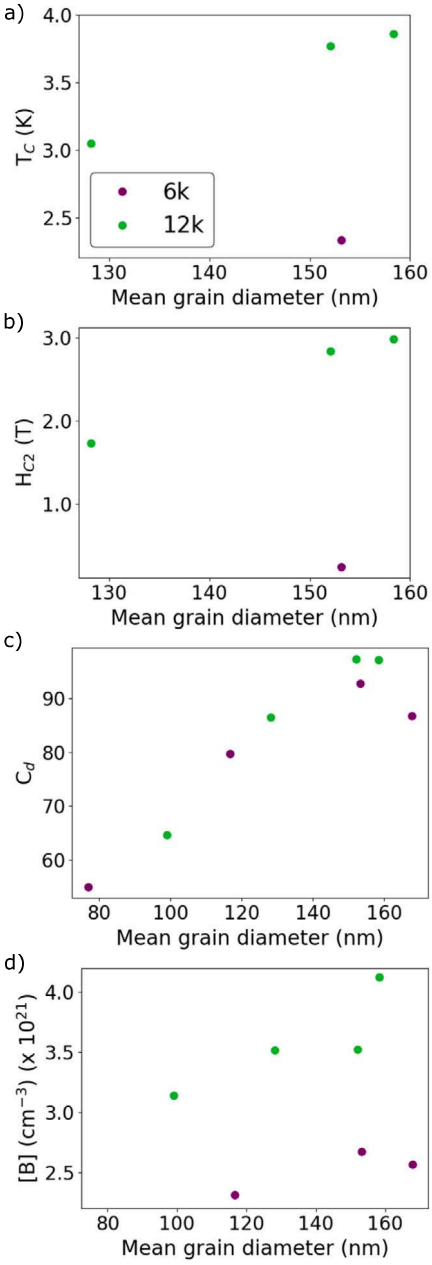

Fig. 7. Critical temperature, upper critical field, C_d and [B] as a function of mean grain diameter for both films. a) T_c as a function of mean grain diameter, **b)** H_{c2} as a function of mean grain diameter, **c)** C_d as a function of mean grain diameter and **d)** [B] as a function of mean grain diameter. The boron concentration for the sample with the smallest mean grain diameter from the 6 k film is not included due to the inaccurate calculated value, which is a result of the weak Raman signal used to determine it.

temperature decreases while moving outwards for both films. Furthermore, no transition was observed over the available measurement range for the outermost region in both samples. A similar behaviour was observed for the critical field as well, wherein, the critical field reduces while moving radially outwards. The underlying explanation for the observed variation in electrical properties was investigated by Raman spectroscopy, XPS, AFM and SEM. Raman spectroscopy indicated a decreasing boron concentration and diamond purity while moving radially outwards for both films. XPS data was then analysed to determine the behaviour in boron concentration and the diamond content in each sample. A significant variation in the film properties measured with Raman and XPS was observed. The observed differences result from the significant variation in the depth profile of Raman and XPS techniques. AFM measurements show a reduction in surface roughness and an increase in the number of grains for samples measured further from the centre, suggesting a variation in film thickness, from thick to thin, while moving radially outwards for both films. SEM analysis showed a shift to smaller grain areas for samples measured further away from the film centre in both films. This analysis shows how the grain distributions differ depending on the distance from the centre and further suggests a reduction in film thickness. The decrease in T_c and H_{c2} in the films, while moving outwards from the centre, can be attributed to a combination of a decrease in boron concentration, diamond purity, and grain size. The results from this study clearly show that the best part of a BNCD film for device fabrication is the central 20–25 mm in a two-inch diameter film. The usable area in the film can be improved by changing the growth conditions to increase uniformity over large areas. Considering the geometry of the growth chamber and the upper limit on the microwave power density, however, this may require a completely new set of growth conditions and will form the basis of future studies.

CRediT authorship contribution statement

J.J. Bennett: Writing – review & editing, Writing – original draft, Methodology, Investigation, Formal analysis, Data curation. **S. Mandal:** Writing – review & editing, Supervision, Methodology, Investigation, Data curation, Conceptualization. **D.J. Morgan:** Resources, Formal analysis. **A. Papageorgiou:** Formal analysis, Resources. **O.A. Williams:** Funding acquisition, Resources. **G.M. Klemencic:** Funding acquisition, Conceptualization, Project administration, Data curation, Writing – review & editing, Supervision.

Declaration of competing interest

The authors declare the following financial interests/personal relationships which may be considered as potential competing interests: Jake James Bennett reports financial support was provided by Engineering and Physical Sciences Research Council. If there are other authors, they declare that they have no known competing financial interests or personal relationships that could have appeared to influence the work reported in this paper.

Data availability

The datasets generated and/or analysed during this study can be found at: https://doi.org/10.17035/d.2023.0297238455.

Declaration of generative AI and AI-assisted technologies in the writing process

During the preparation of this work the author used ChatGPT 3.5 in order to improve readability. After using this tool, the author reviewed and edited the content as needed and takes full responsibility for the content of the publication.

Acknowledgements

The authors gratefully acknowledge the financial support received from the EPSRC Centre for Doctoral Training, United Kingdom Grant No. EP/W524682. XPS data collection was performed at the EPSRC National Facility for XPS ('HarwellXPS'), operated by Cardiff University and UCL, under contract No. PR16195.

Appendix A. Supplementary material

Supplementary material related to this article can be found online at https://doi.org/10.1016/j.cartre.2024.100353.

References

[1] J. Field, The mechanical and strength properties of diamond, Rep. Prog. Phys. 75 (12) (2012) 126505, https://doi.org/10.1088/0034-4885/75/12/126505.
[2] E. Ekimov, V. Sidorov, E. Bauer, N. Mel'Nik, N. Curro, J. Thompson, S. Stishov, Superconductivity in diamond, Nature 428 (6982) (2004) 542–545, https://doi.org/10.1038/nature02449.
[3] W. Gajewski, P. Achatz, O. Williams, K. Haenen, E. Bustarret, M. Stutzmann, J. Garrido, Electronic and optical properties of boron-doped nanocrystalline diamond films, Phys. Rev. B 79 (4) (2009) 045206, https://doi.org/10.1103/PhysRevB.79.045206.
[4] Y. Takano, M. Nagao, T. Takenouchi, H. Umezawa, I. Sakaguchi, M. Tachiki, H. Kawarada, Superconductivity in polycrystalline diamond thin films, Diam. Relat. Mater. 14 (2005) 1936–1938, https://doi.org/10.1016/j.diamond.2005.08.014.
[5] B. Willems, G. Zhang, J. Vanacken, V. Moshchalkov, S. Janssens, K. Haenen, P. Wagner, Granular superconductivity in metallic and insulating nanocrystalline boron-doped diamond thin films, J. Phys. D, Appl. Phys. 43 (37) (2010) 374019, https://doi.org/10.1088/0022-3727/43/37/374019.
[6] J.A. Cuenca, T. Brien, S. Mandal, S. Manifold, S. Doyle, A. Porch, G.M. Klemencic, O.A. Williams, Superconducting boron doped nanocrystalline diamond microwave coplanar resonator, Carbon 201 (2023) 251–259, https://doi.org/10.1016/j.carbon.2022.08.084.
[7] S. Mandal, T. Bautze, O.A. Williams, C. Naud, É. Bustarret, F. Omnes, P. Rodiere, T. Meunier, C. Baüerle, L. Saminadayar, The diamond superconducting quantum interference device, ACS Nano 5 (9) (2011) 7144–7148, https://doi.org/10.1021/nn2018396.
[8] M. Bose, D.L. Creedon, A. Barlow, M. Stuiber, G.M. Klemencic, S. Mandal, O. Williams, G. van Riessen, C.I. Pakes, Low-noise diamond-based dc nano-squids, ACS Appl. Electron. Mater. 4 (5) (2022) 2246–2252, https://doi.org/10.1021/acsaelm.2c00048.
[9] R. Bogdanowicz, M. Sobaszek, M. Ficek, D. Kopiec, M. Moczała, K. Orłowska, M. Sawczak, T. Gotszalk, Fabrication and characterization of boron-doped nanocrystalline diamond-coated mems probes, Appl. Phys. A 122 (2016) 1–9, https://doi.org/10.1007/s00339-016-9829-9.
[10] T. Bautze, S. Mandal, O.A. Williams, P. Rodiere, T. Meunier, C. Bäuerle, Superconducting nano-mechanical diamond resonators, Carbon 72 (2014) 100–105, https://doi.org/10.1016/j.carbon.2014.01.060.
[11] M. Sobaszek, R. Bogdanowicz, K. Siuzdak, A. Cirocka, P. Zięba, M. Gnyba, M. Naparty, P. Płotka, et al., Optical and electrical properties of ultrathin transparent nanocrystalline boron-doped diamond electrodes, Opt. Mater. 42 (2015) 24–34, https://doi.org/10.1016/j.optmat.2014.12.014.
[12] Z.J. Ayres, J.C. Newland, M.E. Newton, S. Mandal, O.A. Williams, J.V. Macpherson, Impact of chemical vapour deposition plasma inhomogeneity on the spatial variation of sp2 carbon in boron doped diamond electrodes, Carbon 121 (2017) 434–442, https://doi.org/10.1016/j.carbon.2017.06.008.
[13] S. Garcia-Segura, E.V. Dos Santos, C.A. Martínez-Huitle, Role of sp3/sp2 ratio on the electrocatalytic properties of boron-doped diamond electrodes: a mini review, Electrochem. Commun. 59 (2015) 52–55, https://doi.org/10.1016/j.elecom.2015.07.002.
[14] J.A. Bennett, J. Wang, Y. Show, G.M. Swain, Effect of sp2-bonded nondiamond carbon impurity on the response of boron-doped polycrystalline diamond thin-film electrodes, J. Electrochem. Soc. 151 (9) (2004) E306, https://doi.org/10.1149/1.1780111.
[15] Y. Feng, J. Lv, J. Liu, N. Gao, H. Peng, Y. Chen, Influence of boron concentration on growth characteristic and electro-catalytic performance of boron-doped diamond electrodes prepared by direct current plasma chemical vapor deposition, Appl. Surf. Sci. 257 (8) (2011) 3433–3439, https://doi.org/10.1016/j.apsusc.2010.11.041.
[16] P. Yu, J. Zhang, T. Zheng, T. Wang, Influence of boron doped level on the electrochemical behavior of boron doped diamond electrodes and uric acid detection, Colloids Surf. A, Physicochem. Eng. Asp. 494 (2016) 241–247, https://doi.org/10.1016/j.colsurfa.2016.01.031.
[17] J. Zhao, J. Wang, J. Zhi, Z. Zhang, Preparation of grain size controlled boron-doped diamond thin films and their applications in selective detection of glucose in basic solutions, Sci. China Chem. 53 (2010) 1378–1384, https://doi.org/10.1007/s11426-010-3099-8.
[18] G. Zhang, S. Janssens, J. Vanacken, M. Timmermans, J. Vacík, G. Ataklti, W. Decelle, W. Gillijns, B. Goderis, K. Haenen, et al., Role of grain size in superconducting boron-doped nanocrystalline diamond thin films grown by cvd, Phys. Rev. B 84 (21) (2011) 214517, https://doi.org/10.1103/PhysRevB.84.214517.
[19] C. Lu, S. Tian, C. Gu, J. Li, Grain boundary effect on the superconducting transition of microcrystalline boron-doped diamond films, Diam. Relat. Mater. 20 (2) (2011) 217–220, https://doi.org/10.1016/j.diamond.2010.12.003.
[20] G.M. Klemencic, J.M. Fellows, J.M. Werrell, S. Mandal, S.R. Giblin, R.A. Smith, O.A. Williams, Fluctuation spectroscopy as a probe of granular superconducting diamond films, Phys. Rev. Mater. 1 (4) (2017) 044801, https://doi.org/10.1103/PhysRevMaterials.1.044801.
[21] H.A. Bland, E.L. Thomas, G.M. Klemencic, S. Mandal, D.J. Morgan, A. Papageorgiou, T.G. Jones, O.A. Williams, Superconducting diamond on silicon nitride for device applications, Sci. Rep. 9 (1) (2019) 2911, https://doi.org/10.1038/s41598-019-39707-z.
[22] Q.-Y. Tong, G. Fountain, P. Enquist, Room temperature SiO2/SiO2 covalent bonding, Appl. Phys. Lett. 89 (4) (2006) 042110, https://doi.org/10.1063/1.2240232.
[23] W.D. Harkins, Energy relations of the surface of solids I. Surface energy of the diamond, J. Chem. Phys. 10 (5) (1942) 268–272, https://doi.org/10.1063/1.1723719.
[24] O.A. Williams, O. Douhéret, M. Daenen, K. Haenen, E. Ōsawa, M. Takahashi, Enhanced diamond nucleation on monodispersed nanocrystalline diamond, Chem. Phys. Lett. 445 (4–6) (2007) 255–258, https://doi.org/10.1016/j.cplett.2007.07.091.
[25] S. Mandal, Nucleation of diamond films on heterogeneous substrates: a review, RSC Adv. 11 (2021) 10159–10182, https://doi.org/10.1039/D1RA00397F.
[26] N. Fairley, V. Fernandez, M. Richard-Plouet, C. Guillot-Deudon, J. Walton, E. Smith, D. Flahaut, M. Greiner, M. Biesinger, S. Tougaard, et al., Systematic and collaborative approach to problem solving using X-ray photoelectron spectroscopy, Appl. Surf. Sci. Adv. 5 (2021) 100112, https://doi.org/10.1016/j.apsadv.2021.100112.
[27] P. Achatz, E. Bustarret, C. Marcenat, R. Piquerel, T. Dubouchet, C. Chapelier, A. Bonnot, O. Williams, K. Haenen, W. Gajewski, J. Garrido, M. Stutzmann, Metal–insulator transition and superconductivity in highly boron-doped nanocrystalline diamond films, Phys. Status Solidi A 206 (9) (2009) 1978–1985, https://doi.org/10.1002/pssa.200982233.
[28] V. Mortet, A. Taylor, Z.V. Živcová, D. Machon, O. Frank, P. Hubík, D. Trémouilles, L. Kavan, Analysis of heavily boron-doped diamond Raman spectrum, Diam. Relat. Mater. 88 (2018) 163–166.
[29] P. Szirmai, T. Pichler, O.A. Williams, S. Mandal, C. Bäuerle, F. Simon, A detailed analysis of the Raman spectra in superconducting boron doped nanocrystalline diamond, Phys. Status Solidi B 249 (12) (2012) 2656–2659, https://doi.org/10.1002/pssb.201200461.
[30] V. Sidorov, E. Ekimov, Superconductivity in diamond, Diam. Relat. Mater. 19 (5–6) (2010) 351–357, https://doi.org/10.1016/j.diamond.2009.12.002.
[31] V. Mortet, Z.V. Živcová, A. Taylor, O. Frank, P. Hubík, D. Trémouilles, F. Jomard, J. Barjon, L. Kavan, Insight into boron-doped diamond Raman spectra characteristic features, Carbon 115 (2017) 279–284, https://doi.org/10.1016/j.carbon.2017.01.022.
[32] S. Prawer, R.J. Nemanich, Raman spectroscopy of diamond and doped diamond, Philos. Trans. R. Soc. Lond. A, Math. Phys. Eng. Sci. 362 (1824) (2004) 2537–2565, https://doi.org/10.1098/rsta.2004.1451.
[33] F. Pruvost, A. Deneuville, Analysis of the Fano in diamond, Diam. Relat. Mater. 10 (3) (2001) 531–535, https://doi.org/10.1016/S0925-9635(00)00378-2.
[34] A.C. Ferrari, J. Robertson, Resonant Raman spectroscopy of disordered, amorphous, and diamondlike carbon, Phys. Rev. B 64 (7) (2001) 075414, https://doi.org/10.1103/PhysRevB.64.075414.
[35] J.A. Cuenca, S. Mandal, E.L.H. Thomas, O.A. Williams, Microwave plasma modelling in clamshell chemical vapour deposition diamond reactors, Diam. Relat. Mater. 124 (2022) 108917, https://doi.org/10.1016/j.carbon.2022.08.084.
[36] V. Volodin, V. Mortet, A. Taylor, Z. Remes, T. Stuchliková, J. Stuchlik, Raman scattering in boron doped nanocrystalline diamond films: manifestation of Fano interference and phonon confinement effect, Solid State Commun. 276 (2018) 33–36, https://doi.org/10.1016/j.ssc.2018.04.004.
[37] J.W. Ager III, M.D. Drory, Quantitative measurement of residual biaxial stress by Raman spectroscopy in diamond grown on a Ti alloy by chemical vapor deposition, Phys. Rev. B 48 (4) (1993) 2601, https://doi.org/10.1103/PhysRevB.48.2601.

[38] W. Wang, M. Polo, G. Sanchez, J. Cifre, J. Esteve, Internal stress and strain in heavily boron-doped diamond films grown by microwave plasma and hot filament chemical vapor deposition, J. Appl. Phys. 80 (3) (1996) 1846–1850, https://doi.org/10.1063/1.362996.

[39] N. Ferreira, E. Abramof, E. Corat, V. Trava-Airoldi, Residual stresses and crystalline quality of heavily boron-doped diamond films analysed by micro-Raman spectroscopy and X-ray diffraction, Carbon 41 (6) (2003) 1301–1308, https://doi.org/10.1016/S0008-6223(03)00071-X.

[40] B. Dec, M. Ficek, M. Rycewicz, Łukasz Macewicz, M. Gnyba, M. Sawczak, M. Sobaszek, R. Bogdanowicz, Gas composition influence on the properties of boron-doped diamond films deposited on the fused silica, Mater. Sci.-Poland 36 (2) (2018) 288–296, https://doi.org/10.2478/msp-2018-0046.

[41] M. Bernard, A. Deneuville, P. Muret, Non-destructive determination of the boron concentration of heavily doped metallic diamond thin films from Raman spectroscopy, Diam. Relat. Mater. 13 (2) (2004) 282–286, https://doi.org/10.1016/j.diamond.2003.10.051.

[42] V. Mortet, Z.V. Živcová, A. Taylor, O. Frank, P. Hubík, D. Trémouilles, F. Jomard, J. Barjon, L. Kavan, Insight into boron-doped diamond Raman spectra characteristic features, Carbon 115 (2017) 279–284, https://doi.org/10.1016/j.carbon.2017.01.022.

[43] R. Rouzbahani, S.S. Nicley, D.E. Vanpoucke, F. Lloret, P. Pobedinskas, D. Araujo, K. Haenen, Impact of methane concentration on surface morphology and boron incorporation of heavily boron-doped single crystal diamond layers, Carbon 172 (2021) 463–473, https://doi.org/10.1016/j.carbon.2020.10.061.

[44] S. Janssens, P. Pobedinskas, J. Vacik, V. Petráková, B. Ruttens, J. D'Haen, M. Nesládek, K. Haenen, P. Wagner, Separation of intra- and intergranular magnetotransport properties in nanocrystalline diamond films on the metallic side of the metal–insulator transition, New J. Phys. 13 (8) (2011) 083008, https://doi.org/10.1088/1367-2630/13/8/083008.

[45] D. Kumar, S. Samanta, K. Sethupathi, M.R. Rao, Flux pinning and improved critical current density in superconducting boron doped diamond films, J. Phys. Commun. 2 (4) (2018) 045015, https://doi.org/10.1088/2399-6528/aab39f.

[46] S.D. Janssens, P. Pobedinskas, V. Petráková, M. Nesládek, K. Haenen, P. Wagner, Influence of methane concentration on the electric transport properties in heavily boron-doped nanocrystalline CVD diamond films, MRS Proc. 1282 (2011), https://doi.org/10.1557/opl.2011.454, mrsf10–1282–a15–04.

[47] J.F. Moulder, W.F. Stickle, P.E. Sobol, K.D. Bomben, Handbook of X-Ray Photoelectron Spectroscopy: A Reference Book of Standard Spectra for Identification and Interpretation of XPS Data, Physical Electronics Division, Perkin-Elmer Corporation, 1992.

[48] M. Sobaszek, K. Siuzdak, J. Ryl, M. Sawczak, S. Gupta, S. Carrizosa, M. Ficek, B. Dec, K. Darowicki, R. Bogdanowicz, Diamond phase (sp3-c) rich boron-doped carbon nanowalls (sp2-c): physicochemical and electrochemical properties, J. Phys. Chem. C 121 (38) (2017) 20821–20833, https://doi.org/10.1021/acs.jpcc.7b06365.

[49] C.R. Brundle, C.A. Evans, S. Wilson, Encyclopedia of Materials Characterization, Elsevier, 1992.

[50] M. Volmer, A. Weber, Keimbildung in übersättigten Gebilden, Z. Phys. Chem. 119U (1) (1926) 277–301, https://doi.org/10.1515/zpch-1926-11927.

[51] X. Jiang, K. Schiffmann, C.-P. Klages, Nucleation and initial growth phase of diamond thin films on (100) silicon, Phys. Rev. B 50 (12) (1994) 8402–8410, https://doi.org/10.1103/PhysRevB.50.8402.

[52] A. Van der Drift, Evolutionary selection, a principle governing growth orientation in vapour-deposited layers, Philips Res. Rep. 22 (3) (1967) 267.

[53] O.A. Williams, Nanocrystalline diamond, Diam. Relat. Mater. 20 (5–6) (2011) 621–640, https://doi.org/10.1016/j.diamond.2011.02.015.

[54] X. Jiang, G. Yu, S. Lee, Simulation of polycrystalline 3D film growth: an investigation of the evolution of grain size and texture in diamond films, Appl. Phys. A, Mater. Sci. Process. 74 (2) (2002) 217–224, https://doi.org/10.1007/s003390100869.

[55] S. Kitagoh, R. Okada, A. Kawano, M. Watanabe, Y. Takano, T. Yamaguchi, T. Chikyow, H. Kawarada, Cross-sectional tem study and film thickness dependence of tc in heavily boron-doped superconducting diamond, Physica C, Supercond. Appl. 470 (2010) S610–S612, https://doi.org/10.1016/j.physc.2009.12.064.

[56] G. Zhang, S. Turner, E.A. Ekimov, J. Vanacken, M. Timmermans, T. Samuely, V.A. Sidorov, S.M. Stishov, Y. Lu, B. Deloof, et al., Global and local superconductivity in boron-doped granular diamond, Adv. Mater. 26 (13) (2014) 2034–2040.

[57] M. Tsigkourakos, T. Hantschel, S.D. Janssens, K. Haenen, W. Vandervorst, Spin-seeding approach for diamond growth on large area silicon-wafer substrates, Phys. Status Solidi A 209 (9) (2012) 1659–1663, https://doi.org/10.1002/pssa.201200137.